Multiscale Photoacoustic Microscopy of Single-Walled Carbon Nanotube-Incorporated Tissue Engineering Scaffolds

Xin Cai, M.Sc.,[1,*] Bhavna S. Paratala, M.Sc.,[2,*] Song Hu, Ph.D.,[1,*]
Balaji Sitharaman, Ph.D.,[2] and Lihong V. Wang, Ph.D.[1]

Three-dimensional polymeric scaffolds provide structural support and function as substrates for cells and bioactive molecules necessary for tissue regeneration. Noninvasive real-time imaging of scaffolds and/or the process of tissue formation within the scaffold remains a challenge. Microcomputed tomography, the widely used technique to characterize polymeric scaffolds, shows poor contrast for scaffolds immersed in biological fluids, thereby limiting its utilities under physiological conditions. In this article, multiscale photoacoustic microscopy (PAM), consisting of both acoustic-resolution PAM (AR-PAM) and optical-resolution PAM (OR-PAM), was employed to image and characterize single-walled carbon-nanotube (SWNT)–incorporated poly(lactic-co-glycolic acid) polymer scaffolds immersed in biological buffer. SWNTs were incorporated to reinforce the mechanical properties of the scaffolds, and to enhance the photoacoustic signal from the scaffolds. By choosing excitation wavelengths of 570 and 638 nm, multiscale PAM could spectroscopically differentiate the photoacoustic signals generated from blood and from carbon-nanotube-incorporated scaffolds. OR-PAM, providing a fine lateral resolution of 2.6 μm with an adequate tissue penetration of 660 μm, successfully quantified the average porosity and pore size of the scaffolds to be 86.5% ± 1.2% and 153 ± 15 μm in diameter, respectively. AR-PAM further extended the tissue penetration to 2 mm at the expense of lateral resolution (45 μm). Our results suggest that PAM is a promising tool for noninvasive real-time imaging and monitoring of tissue engineering scaffolds *in vitro*, and *in vivo* under physiological conditions.

Introduction

THREE-DIMENSIONAL (3D) porous polymeric scaffolds are important components in the development of tissue engineering strategies that provide structural support, and carry cells as well as growth factors to improve, maintain, or replace tissue or organ function. Thus, they must possess important characteristics such as good biocompatibility with surrounding tissue, adequate mechanical properties, large porosity, proper pore size, and high pore interconnectivity for tissue in-growth, and biodegradability that permits the scaffold to be gradually replaced by growing tissue.[1] The most widely used techniques to assess polymeric scaffold characteristics such as porosity and pore size are mercury porosimetry, scanning electron microscopy (SEM), laser scanning optical microscopy techniques (e.g., confocal and two-photon microscopy), and X-ray microcomputed tomography (micro-CT). However, these techniques have limitations. While mercury porosimetry and SEM are invasive, laser scanning optical microscopy techniques have limited

tissue penetration (tens of micrometers) especially in the presence of blood due to strong light scattering. X-ray micro-CT can penetrate a whole polymeric construct up to several centimeters, and allows noninvasive assessment of dry polymeric scaffolds. However, when the polymeric scaffolds are immersed in fluids or biological media such as blood, or embedded *in vivo*, wherein fluids perfuse through the scaffolds, the micro-CT images show poor contrast. Thus, new tools and techniques with high resolution, deep penetration, and high contrast are needed that allow noninvasive imaging, and monitoring of changes in scaffold characteristics such as porosity, pore size, or degradation.[2]

Photoacoustic microscopy (PAM) is a promising tool for tissue engineering, and has recently been reported to allow noninvasive imaging of cells seeded, and distributed on polymeric scaffolds *in vitro*.[3] PAM detects photoacoustic waves generated from objects that absorb either pulsed or intensity-modulated laser irradiation.[4] In contrast to the ionizing X-ray micro-CT, the nonionizing photonic irradiation in PAM imaging is not hazardous to tissues.

---

[1]Optical Imaging Laboratory, Department of Biomedical Engineering, Washington University in St. Louis, St. Louis, Missouri.
[2]Department of Biomedical Engineering, State University of New York at Stony Brook, Stony Brook, New York.
*These three authors contributed equally to this work.

Additionally, PAM is capable of multiscale imaging, covering a wide spatial region spanning from organelles to organs.[5] With weakly focused optical illumination, acoustic-resolution photoacoustic microscopy (AR-PAM) has demonstrated multi-millimeter *in vivo* penetration with tissue level resolution (45 μm).[6] Utilizing diffraction-limited optical focusing, optical-resolution photoacoustic microscopy (OR-PAM) has achieved cellular level resolution *in vivo*.[7] Recently, single-walled carbon nanotubes (SWNTs)—reinforced polymer nanocomposites and scaffolds—have been investigated for tissue engineering applications.[8–10] SWNTs have also been developed as contrast agents for various imaging techniques, including photoacoustic imaging.[11,12] In this work, for the first time, we have applied multiscale PAM to demonstrate its efficacy to noninvasively image, and characterize SWNT-incorporated poly (D, L-lactide-co-glycolide) (PLGA) polymer scaffolds in blood and tissue phantoms.

Materials and Methods

SWNT synthesis

The method of diblock copolymer templating was used to coat Fe on Si wafers. The wafers were placed in a 3-inch-diameter quartz reaction chamber (Easy Tube 2000; First Nano) and heated in Ar to 900°C. To initiate the growth of SWNTs, the chamber was filled with H_2 for 2 min, and CH_4 was added to the gas flow as the carbon feedstock for 20 min. Subsequently, the carbon feedstock was switched off and the furnace was cooled to room temperature.[11,13]

Preparation of SWNT-incorporated PLGA scaffolds

An established procedure of high shear mixing, sonicating, and drying was used to prepare porous SWNT-incorporated PLGA scaffolds.[10] The nanotubes were uniformly distributed in the PLGA (Polysciences, Inc.) mixture at 0.5 wt% concentration. This wt% was chosen since previous studies show that SWNT-incorporated polymer composites achieved their maximum mechanical properties at this loading concentration.[8] Porous SWNT-incorporated scaffolds were fabricated by a thermal-crosslinking particulate-leaching technique with NaCl porogen (size range: 100–500 μm).[10] To achieve 90% porosity, the amount of NaCl was calculated using the equation:

$$Porosity = \frac{W_{NaCl}}{W_{PLGA} + W_{SWNT} + W_{NaCl}} \times 100\%$$

where W_{PLGA}, W_{SWNT}, and W_{NaCl} are the weight of PLGA, SWNT, and NaCl, respectively. The mixture was then poured into cylindrical Teflon™ molds of 4 mm in diameter and 1.5 mm in height. The scaffolds were then immersed in scintillation vials filled with deionized water (changed every 6 h) and the vials were kept on a shaker table (80 rpm) continuously for 48 h to leach out the NaCl. Finally, the scaffolds were blotted and dried at room temperature for 24 h.

Electron microscopy and atomic force microscopy

To characterize the SWNT structure, transmission electron microscopy (TEM; Tecnai12 BioTwinG2) was performed at an accelerating voltage of 80 kV. SWNT samples were prepared by mounting them on a 400-mesh copper grid with Formvar coating. In addition, atomic force microscopy (AFM, MFD-3D-BIO; Asylum Research) was also performed.

The PLGA polymer scaffold structure was examined by SEM (Schottky Field Emission Scanning Electron Microscope, LEO Gemini 1550), which was performed at an accelerating voltage of 20 kV with an Everhart-Thornley secondary electron detector. The porous scaffolds in their dry form were sliced, mounted on metal studs, and sputter coated with gold for imaging.

Microcomputed tomography

The dry and wet (immersed in fetal bovine serum) SWNT-incorporated PLGA polymer scaffolds were imaged using a desktop micro-CT scanner (micro-CT 40; Scanco Medical AG) at 12 μm resolution, with an energy of 55 kV and intensity of 145 μA. Image reconstruction and analysis was carried out by the software provided by the Scanco Medical AG. A threshold value of 41 was chosen to represent the gray scale tomograms of the scaffolds by their binary counterparts in all the image reconstructions and quantitative analysis in this study.

Photoacoustic microscopy

Figure 1 shows a schematic of the multiscale PAM system. Optical excitation is induced by a dye laser (pulse width:

FIG. 1. Schematic of the reflection-mode AR-PAM and OR-PAM systems. A Cartesian coordinate is also shown in the drawing. CL, conical lens; CorL, correction lens; MMF, multimode fiber; Obj, objective; OC, optical condenser; PD, photodiode; RAP, right-angle prism; RhP, rhomboid prism; SMF, single-mode fiber; SO, silicone oil; US, ultrasonic transducer; AR-PAM, acoustic-resolution photoacoustic microscopy; OR-PAM, optical-resolution photoacoustic microscopy. Color images available online at www.liebertonline.com/tec
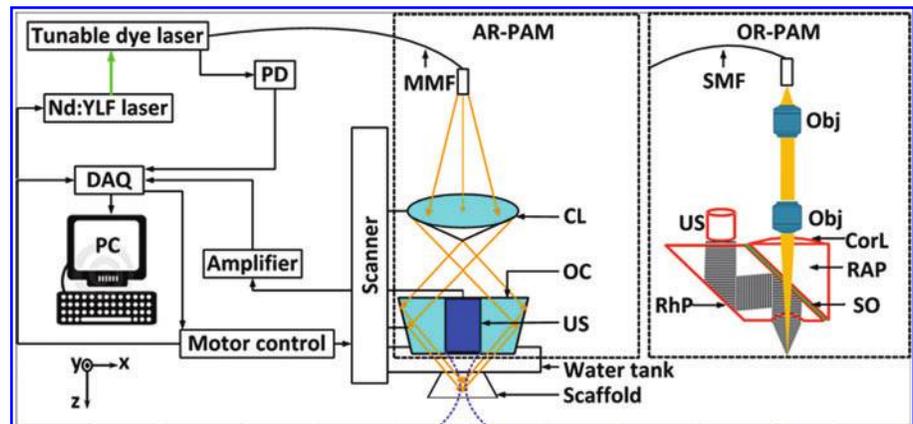
7 ns; repetition rate: 5 kHz; CBR-D) pumped by a Nd:YLF laser (INNOSLAB; Edgewave), and the generated acoustic wave is detected by a focused ultrasonic transducer. In PAM, the optical and ultrasonic foci are configured coaxially and confocally, and the lateral resolution is predominantly determined by the more tightly focused one. The axial resolution and the maximum penetration depth are inversely proportional to the center frequency of the transducer.[14] A photodiode measured the energy of each laser pulse for signal calibration. The transducer surface is immersed in water for ultrasound coupling. An imaging window in the bottom of the water tank is sealed with an ultrasonically, and optically transparent polyethylene membrane. Ultrasonic gel is applied between the imaging window and samples for ultrasound coupling.

For AR-PAM, the light is coupled into a multimode optical fiber (M30L02; Thorlabs) and reshaped by a conical lens to form a ring pattern. The ring-shaped light pattern is then weakly focused into the sample by an optical condenser. The optical focus is 2 mm in diameter, much wider than the 45-μm ultrasonic focus.[6,15] Using a focused ultrasonic transducer with 50 MHz central frequency (V214-BB-RM; Olympus NDT), AR-PAM can achieve 45-μm lateral resolution, 15-μm axial resolution, and more than 3-mm penetration depth.

For OR-PAM, bright-field optical illumination, much smaller in diameter than the acoustic focus, is adopted to achieve optical resolution.[16] The output of the single-mode fiber (P1-460A-FC-2; Thorlabs) is collimated by a microscope objective (RMS4X; Thorlabs), and fills the back aperture of another identical objective (imaging objective) to achieve nearly diffraction-limited optical focusing. A right-angle prism and a rhomboid prism (NT49-419; Edmund Optics) sandwich a thin layer of silicone oil for acoustic-optical coaxial alignment. The lateral resolution of OR-PAM was 2.6 μm, sufficient to resolve microvasculature as small as single capillaries.[7] However, the tissue penetration of OR-PAM was restricted to ~1 mm due to the high optical scattering.[17]

A 1D depth-resolved image (A-line, defined as the z direction) is obtained by measuring the time-resolved photoacoustic signal at each scanned location. The 1D raster scanning, consisting of multiple A-lines, provides a 2D B-scan image. Two-dimensional raster scanning along the transverse plane (x-y plane) further provides a 3D visualization of the optical absorption property of the imaging target. The acquired volumetric image can be viewed in either maximum amplitude projection (MAP) or direct 3D rendering. MAP is performed by projecting the maximum signal from each A-line onto the corresponding x-y plane, and direct 3D rendering is processed by Volview software (Kitware, Inc.). All photoacoustic data are collected and processed by user-defined LabView (National Instruments) and MATLAB (MathWorks, Inc.) programs.

Quantification of scaffold porosity and pore size

The porosity of the scaffold is defined as the complement of the scaffold volume fraction (porosity = 1 − scaffold volume fraction). The scaffold volume fraction is the ratio of segmented scaffold volume to the total volume in a region of interest (ROI). To evaluate the capability of PAM for measuring porosity and pore size in polymeric PLGA scaffolds incorporating SWNTs, multiscale PAM was performed on four scaffolds. Volumetric data obtained from PAM were processed by MATLAB. For porosity measurements, we counted the number of pixels without photoacoustic signal in the ROI by setting a threshold above the noise level, and then divided it by the total number of pixels. For the micro-CT–based estimation of porosity and pore size, the porous architecture was quantitatively determined by using previously established protocols.[10]

Results

PLGA scaffolds incorporating SWNTs

Figure 2a shows a representative bright-field TEM image of bundled SWNTs. Figure 2b displays a representative high-resolution AFM image of individual SWNTs with diameters between 1 and 2 nm. Figure 2c displays a representative SEM image of the fracture surface of porous PLGA SWNT-incorporated scaffold with the SWNTs drawn out of the polymer matrix and covered by polymer. The SEM micrograph shows the porous architecture, where the bold yellow arrow indicates the PLGA and the dotted yellow arrow points out the SWNTs incorporated within the scaffold. The SEM images further confirmed that SWNTs were well-dispersed in the PLGA polymer. The SEM images of porous PLGA scaffold containing the SWNTs are different than PLGA scaffolds alone. This difference is due to the presence of the SWNTs. Previous studies on polymer scaffolds prepared using the salt-leaching technique with SWNTs at the same concentration show that the presence of the SWNTs at these small concentrations does not change the fundamental chemical structure of the polymer, and that its presence affects the scaffold's bulk properties (mechanical and viscoelastic properties).[8–10,18] Additionally, these reports also show that polymer scaffolds with or without SWNTs have similar cytocompatibility and biocompatibility.

Comparison of PAM and micro-CT

Porous SWNT-incorporated PLGA scaffolds were imaged by both PAM and micro-CT for comparison. Figure 3a and b shows the MAP images of a scaffold immersed in water obtained by AR-PAM and OR-PAM, respectively, at the excitation wavelength of 570 nm. Figure 3c shows an optical microscopic image of the scaffold. The common features that can be identified from the images are indicated by matched numbers. Figure 3d shows a 3D depiction of the scaffold acquired by OR-PAM. The images of the scaffold obtained from AR-PAM and OR-PAM (Fig. 3a and b, respectively), especially the high lateral resolution of OR-PAM, show clear details of the scaffold. And the images agree well with that from the optical microscope.

Micro-CT was also performed on dry and wet (immersed in fetal bovine serum) scaffolds. Figure 3e and g shows a reconstructed micro-CT MAP image and 3D depiction of a dry scaffold, with well-resolved porous architecture. Figure 3f and h shows the reconstructed micro-CT MAP and 3D depiction, respectively, of the scaffold immersed in fetal bovine serum. Figure 3e and g clearly shows that in case of a dry scaffold, clear contours and porous structure of the scaffold are visible, and the image is well resolved

allowing quantification of parameters such as porosity and pore size. However, as seen in Figure 3f and h, on immersing the scaffolds in fetal bovine serum, the scaffold architecture cannot be seen. The crevices on the images are due to trapped air pockets in the pores of the immersed scaffolds.

Photoacoustic images in blood and chicken breast tissue

To evaluate the capability of PAM for imaging scaffolds under physiological conditions, we imaged the scaffolds, either immersed in bovine blood (905–250; Quadfive) or
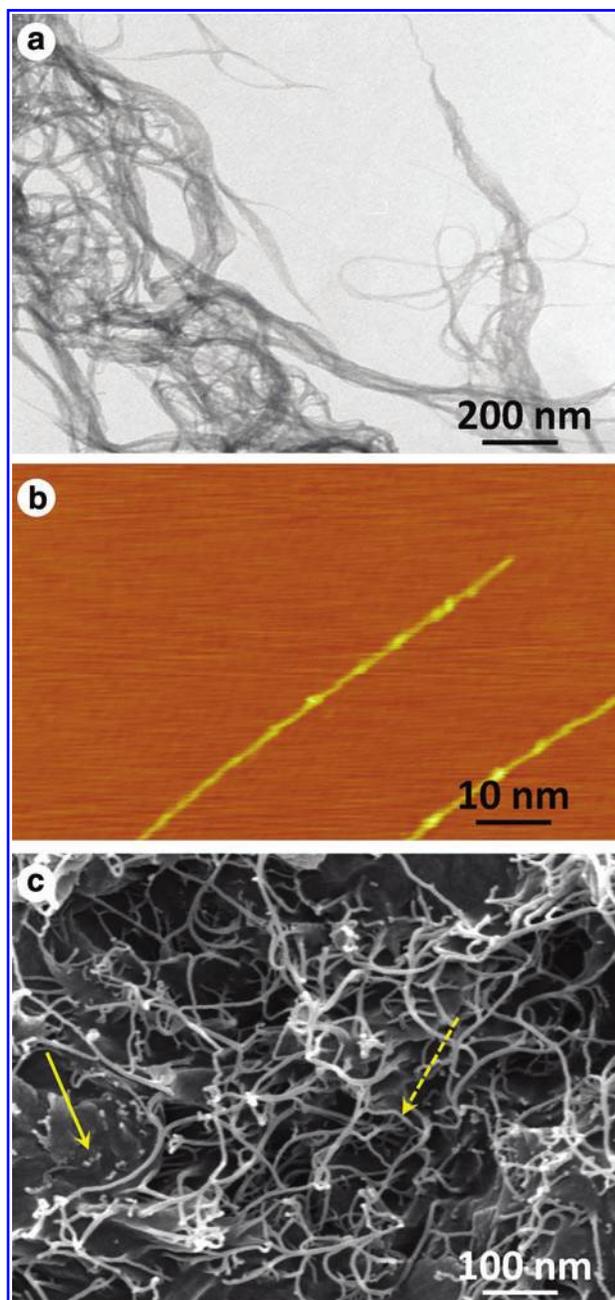
FIG. 2. **(a)** A bright-field transmission electron microscopy image of bundled SWNTs on the surface of the substrate. **(b)** An atomic force microscopy image of two separate SWNTs. **(c)** A scanning electron microscopy image of a porous PLGA scaffold incorporating SWNTs. The bold yellow arrow indicates the PLGA and the dotted yellow arrow points out the SWNTs incorporated within the scaffold. SWNT, single-walled carbon nanotube. PLGA, poly (D, L-lactide-co-glycolide). Color images available online at www .liebertonline.com/tec

FIG. 3. PAM and micro-CT images of the PLGA scaffolds incorporating SWNTs. **(a)** A MAP image of the scaffold by AR-PAM. **(b)** A MAP image of the scaffold by OR-PAM. **(c)** An optical microscope image of the scaffold. The common features that can be identified from the images have matching numbers. **(d)** A 3D depiction of the OR-PAM image. **(e)** A micro-CT MAP image of the scaffold in dry surrounding. **(f)** A micro-CT MAP image of the scaffold in fetal bovine serum. **(g)** A 3D depiction of the micro-CT image in dry surroundings. **(h)** A 3D depiction of the micro-CT image in fetal bovine serum. micro-CT, microcomputed tomography; 3D, three dimensional; MAP, maximum amplitude projection. Color images available online at www.liebertonline.com/tec

embedded in chicken tissue, with our multiscale PAM systems. Initially, the scaffolds were placed in blood. PAM imaging was carried out at two different wavelengths, 570 nm and 638 nm, to spectroscopically differentiate photoacoustic signals received from blood and a SWNT-incorporated scaffold. Figure 4 shows PAM MAP images (Fig. 4a, b, e, f) and corresponding B-scan images (Fig. 4c, d, g, h) of the SWNT-incorporated PLGA polymer scaffold in bovine blood, acquired by multiscale PAM at the two selected wavelengths. At 570 nm (Fig. 4a, c, e, g), PAM does not show the presence of the scaffold when immersed in blood, whereas at 638 nm (Fig. 4b, d, f, h), both AR-PAM and

OR-PAM can produce well-resolved images of the scaffolds. The optical fluence is greatly attenuated by the blood layer at 570 nm, but only slightly attenuated at 638 nm, and is the reason for the variable results at these two wavelengths. In Figure 4b and f, most of the scaffold features can be identified (marked by matched numbers in the images). Comparing AR-PAM images in Figure 4c and d, the 2-mm depth of the scaffold can be clearly visualized because the surface of blood layer and the immersed scaffold are both seen in the coregistered B-scan images.

The same scaffolds were cleaned with ultrapure water, and embedded in chicken tissues cut open using a scalpel
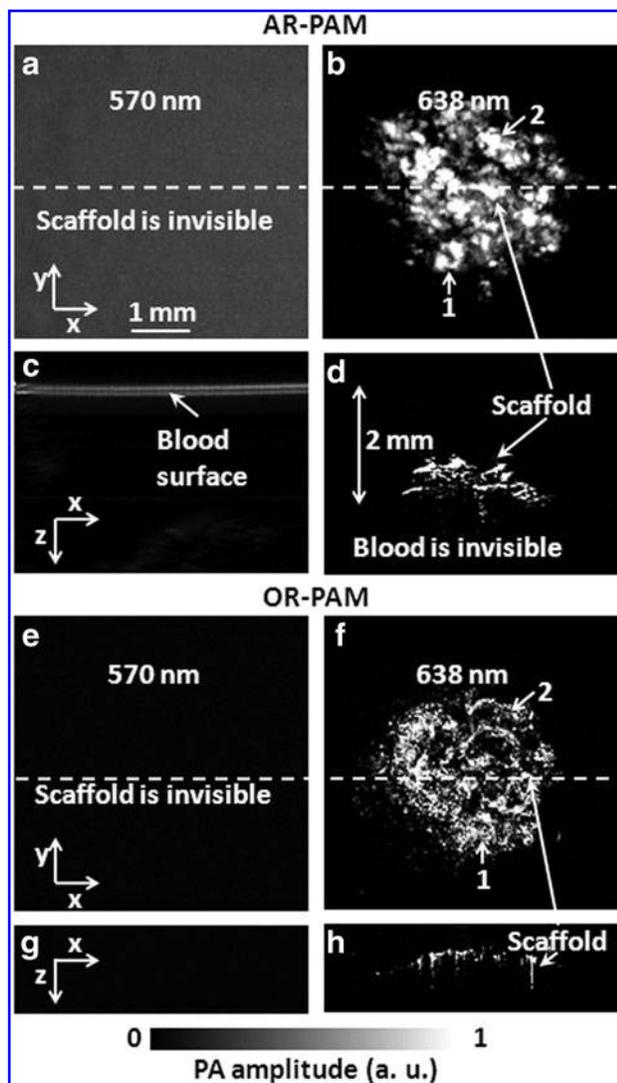
FIG. 4. PAM MAP and B-scan images of the SWNT-incorporating scaffold in bovine blood at different wavelengths. (a) AR-PAM MAP image at 570 nm. (b) AR-PAM MAP image at 638 nm. (c) Corresponding B-scan image at the dash line of (a). (d) Corresponding B-scan image at the dash line of (b), which shows the scaffold ∼2 mm in the blood. (e) OR-PAM MAP image at 570 nm. (f) OR-PAM MAP image at 638 nm. (g) Corresponding B-scan image at the dash line of (e). (h) Corresponding B-scan image at the dash line of (f). The identified scaffold features are marked by matched numbers, which also correspond to the same parts shown in Figure 3.
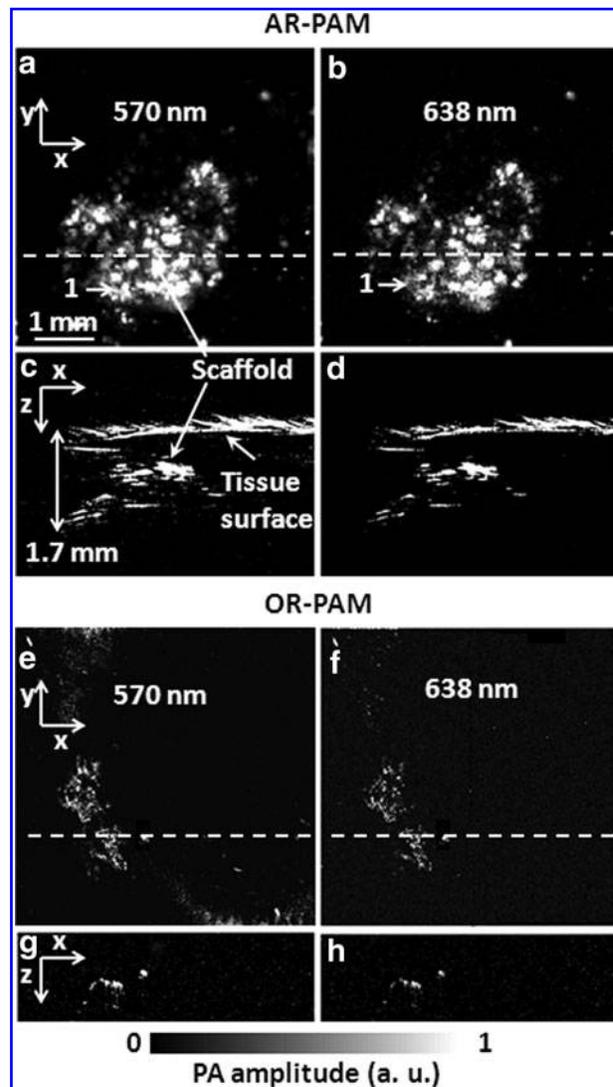
FIG. 5. PAM MAP and B-scan images of the SWNT-incorporating scaffold in chicken breast tissue at different wavelengths. (a) AR-PAM MAP image at 570 nm. (b) AR-PAM MAP image at 638 nm. (c) Corresponding B-scan image at the dashed line of (a). (d) Corresponding B-scan image at the dashed line of (b), which shows the scaffold ∼2 mm in the blood. (e) OR-PAM MAP image at 570 nm. (f) OR-PAM MAP image at 638 nm. (g) Corresponding B-scan image at the dashed line of (e). (h) Corresponding B-scan image at the dashed line of (f). The identified scaffold features are marked by matched numbers, which also correspond to the same parts shown in Figure 3.

blade for multiscale PAM imaging. Figure 5 shows the MAP images (Fig. 5a, b, e, f), and the corresponding B-scan images (Fig. 5c, d, g, h) of the SWNT-incorporated scaffold in chicken breast tissue at the two wavelengths. Figure 5a and b shows that AR-PAM successfully identified some parts of the scaffold in a relatively shallow region (marked by matched numbers in the images). As shown in Figure 5a–d, AR-PAM is able to visualize the scaffold through 1.7-mm-thick tissue layer, and the images well correspond to the images taken in water (Fig. 3a–c) and blood (Fig. 4b, f). In contrast, as seen in Figure 5e–h, OR-PAM can image only a small part of the scaffold in the superficial region.

Quantification of scaffold porosity and pore size

For OR-PAM, the porosity and pore size of the scaffolds were estimated to be 86.5%±1.2% and 153±15 µm (average diameter±standard error, $n=4$), respectively. And for AR-PAM, the porosity and pore size were 81.8%±4.4% and 167±24 µm, respectively. To validate the results, we also imaged the dry scaffolds ($n=4$) by micro-CT. The average porosity of the scaffolds was calculated to be 88.6%±0.8%. An average pore size of 145±9 µm in diameter was obtained. Table 1 shows a comparison of measurements by micro-CT, OR-PAM, and AR-PAM.

Discussion

We have evaluated the ability of multiscale PAM, OR-PAM, and AR-PAM to image tissue engineering scaffolds in simulated physiological environments. The results demonstrate that PAM allows noninvasive imaging, and characterization of the porous structures of wet SWNT-incorporated polymeric scaffolds.

Two wavelengths (570 and 638 nm) were chosen to spectroscopically differentiate the photoacoustic signals generated from blood and from SWNT-incorporated scaffolds. As shown in previous studies, the optical absorption of SWNTs is strong in both the visible and near infrared region.[19] In contrast, the optical absorption of blood is strong in the visible region but relatively weak in the near infrared region.[20] Thus, the 570 nm wavelength was chosen for visualizing both the SWNT-incorporated PLGA scaffolds and blood, while the 638 nm wavelength was selected to differentiate the scaffold signal from the blood signal. In tissue, the embedded scaffold is visible at both wavelengths because the wavelength dependence of fluence attenuation in chicken breast tissue is not as strong as in pure blood. Images (Figs. 3–5) obtained at the two different wavelengths reveal that OR-PAM is capable of achieving better lateral resolution of 2.6 µm, and AR-PAM allows greater imaging depth of more than 1.7 mm for SWNT-incorporated scaffolds immersed in blood or embedded in soft tissue. The AR-PAM system provides adequate resolution at this penetration depth because the resolution is determined by the ultrasound parameters, and ultrasound scattering is much weaker than optical scattering in biological tissues. Photoacoustic tomography can even image deeper at the expense of lateral resolution. By choosing transducer with lower center frequency, photoacoustic systems can image objects in biological tissues as deep as ~5.2 cm,[21,22] which maybe sufficient for the ultimate goals of engineering large volume tissues. Thus, multiscale photoacoustic imaging could potentially become an important link between tissue engineering studies at the microscopic and macroscopic levels. Additionally, PAM allows well-resolved 3D reconstruction of the SWNT-incorporated scaffolds, and quantification of scaffold properties such as porosity and pore size (Table 1). However, PAM is not suitable for imaging dry scaffolds since the generated acoustic signals get attenuated by the air pockets present in their porous architecture. Conversely, micro-CT allows 3D reconstruction and characterization of dry scaffolds, and shows poor contrast for scaffolds immersed in fluids, although emerging X-ray methods can potentially circumvent this issue.[23] Thus, PAM provides complementary and corroborating information compared to micro-CT.

Our results indicate that PAM, in general, is suited for noninvasively imaging, and characterizing *in vitro* tissue engineering scaffolds incorporated with photoacoustic contrast agents under stimulated physiological conditions. Evaluation of scaffold-based strategies for tissue engineering depends on the interaction between biological components (cells and extracellular components) and the physicochemical properties of the scaffold. There is a general consensus that highly porous scaffold structures are required for cellular infiltration, and optimal exchange of nutrients, oxygen, and waste products between the biological components and the surrounding normal tissue. Thus, a large number of *in vitro* studies focus on systematically changing the architecture of the scaffolds, investigating the effects of porosity, pore size, and shape on the adhesion and proliferation characteristics of cells and on oxygen and nutrient diffusions. Widely used tools in these studies include noninvasive imaging techniques such as micro-CT and optical imaging and invasive techniques such as histological analysis. However, each of these tools has limitations. Micro-CT shows poor contrast for scaffolds immersed in biological fluids; optical microscopy is unsuitable in turbid fluids such as blood; and histological analyses require removal of associated cells/tissue and complete drying of the scaffold, which manipulates the scaffold and its environment. Our results suggest that PAM should be able to overcome some of the limitations of noninvasive imaging techniques such as micro-CT and optical imaging and invasive techniques such as histological analysis as well as provide corroborating information for *in vitro* scaffold-based studies.

Our results suggest that OR-PAM and AR-PAM are suitable for imaging photoacoustic contrast agent–incorporated polymeric scaffolds in blood and biological tissue, and should provide useful information about changes in scaffold

TABLE 1. SCAFFOLD POROSITY AND PORE SIZE QUANTIFIED BY OR-PAM, AR-PAM, AND MICROCOMPUTED TOMOGRAPHY

	Porosity (%)	Pore size (µm)
OR-PAM	86.5±1.2	153±15
AR-PAM	81.8±4.4	167±24
Micro-CT	88.6±0.8	145±9

Data are presented as the mean diameter and the standard error ($n=4$).

micro-CT, microcomputed tomography; AR-PAM, acoustic-resolution photoacoustic microscopy; OR-PAM, optical-resolution photoacoustic microscopy.

architecture such as porosity, pore sizes, and degradation effects during tissue regeneration. The fine lateral resolution of 2.6 μm in case of OR-PAM can also be used to nondestructively image *in vitro* the process, and extent of vascularization and angiogenesis. Single capillaries and some vessels have diameters of about 5 μm, and hence formation of new capillaries and interconnectivity of blood vessels, which indicate extent of angiogenesis, can be studied using OR-PAM.[7] Additionally, depending on the tissue engineering application, they show promise to noninvasively image, and characterize scaffolds incorporated with photoacoustic contrast agents *in vivo* in small animals such as mice, rats, and possibly rabbits. Furthermore, photoacoustic imaging could allow noninvasive monitoring of neovascularization,[24] blood flow,[25] and oxygen saturation[6] within tissue engineering scaffolds.

In our investigation, PLGA polymer by itself did not generate sufficient photoacoustic signal to achieve optimum contrast, and thus, small quantities of SWNTs were mixed with the polymer to enhance the photoacoustic signal from the scaffolds. Thus, an important consideration to noninvasively image tissue engineering scaffolds by PAM is that, the scaffold matrix (polymer, ceramic, or metallic biomaterial) should have good absorptive properties (either intrinsically or through incorporation of photoacoustic contrast agents) at the laser wavelength used for PAM.

Conclusions

We have demonstrated multiscale PAM as a promising tool for imaging and characterization of SWNT-incorporated PLGA scaffolds in fluid environment and biological tissues. OR-PAM had better lateral resolution than AR-PAM, and was useful for *ex vivo* quantification of the scaffolds. OR-PAM quantified the average porosity and pore size of the scaffolds to be 86.5% ± 1.2% and 153 ± 15 μm in diameter, respectively. The results agreed well with those measured by micro-CT. However, AR-PAM achieved deeper penetration. In chicken tissue, OR-PAM was defocused and imaged only a small part of the scaffold at superficial depth, whereas AR-PAM still could penetrate the tissue-covered scaffold to 1.7-mm depth. AR-PAM also quantified the average porosity and pore size of the scaffolds to be 81.8% ± 4.4% and 167 ± 24 μm in diameter, respectively. Our results suggest that PAM could overcome some of the limitations of noninvasive imaging techniques such as micro-CT and optical imaging, and invasive techniques such as histological analysis to image and characterize tissue engineering scaffolds.

Acknowledgments

Disclosure Statement

L.V.W. has a financial interest in Microphotoacoustics, Inc., and Endra, Inc., which, however, did not support this work. Others claim no competing financial interests.

References

1. Karageorgiou, V., and Kaplan, D. Porosity of 3D biornaterial scaffolds and osteogenesis. Biomaterials **26,** 5474, 2005.
2. Lovett, M., Lee, K., Edwards, A., and Kaplan, D.L. Vascularization strategies for tissue engineering. Tissue Eng Part B Rev **15,** 353, 2009.
3. Zhang, Y., Cai, X., Choi, S.-W., Kim, C., Wang, L.V., and Xia, Y. Chronic label-free volumetric photoacoustic microscopy of melanoma cells in three-dimensional porous scaffolds. Biomaterials **31,** 8651, 2010.
4. Kim, C., Favazza, C., and Wang, L.V. *In vivo* photoacoustic tomography of chemicals: high-resolution functional and molecular optical imaging at new depths. Chem Rev **110,** 2756, 2010.
5. Wang, L.V. Multiscale photoacoustic microscopy and computed tomography. Nat Photon **3,** 503, 2009.
6. Zhang, H.F., Maslov, K., Stoica, G., and Wang, L.V. Functional photoacoustic microscopy for high-resolution and noninvasive *in vivo* imaging. Nat Biotechnol **24,** 848, 2006.
7. Maslov, K., Zhang, H.F., Hu, S., and Wang, L.V. Optical-resolution photoacoustic microscopy for *in vivo* imaging of single capillaries. Opt Lett **33,** 929, 2008.
8. Sitharaman, B., Shi, X., Tran, L.A., Spicer, P.P., Rusakova, I., Wilson, L.J., *et al.* Injectable *in situ* crosslinkable nanocomposites of biodegradable polymers and carbon nanostructures for bone tissue engineering. J Biomater Sci Polym Ed **18,** 655, 2007.
9. Shi, X., Sitharaman, B., Pham, Q., Hudson, J.L., Wilson, L.J., Tour, J.M., *et al. In vitro* cytotoxicity of single-walled carbon nanotube biodegradable polymer nanocomposites. J Biomed Mater Res Part A **86A,** 813, 2008.
10. Shi, X., Sitharaman, B., Pham, Q.P., Wu, K., Edward Billups, W., Wilson, L.J., *et al.* Fabrication of porous ultra-short single-walled carbon nanotube nanocomposite scaffolds for bone tissue engineering. Biomaterials **28,** 4078, 2007.
11. Pramanik, M., Swierczewska, M., Green, D., Sitharaman, B., and Wang, L.V. Single-walled carbon nanotubes as a multimodal-thermoacoustic and photoacoustic-contrast agent. J Biomed Opt **14,** 034018, 2009.
12. Sitharaman, B., and Wilson, L.J. Gadofullerenes and gadonanotubes: a new paradigm for high-performance MRI contrast agent design. J Biomed Nanotechnol **3,** 342, 2007.
13. Swierczewska, M., Rusakova, I., and Sitharaman, B. Gd and Eu catalysted single-walled carbon nanotube growth. Carbon **47,** 3139, 2009.
14. Hu, S., and Wang, L.V. Neurovascular photoacoustic tomography. Front Neuroenergetics **2,** 10, 2010.
15. Maslov, K., Stoica, G., and Wang, L.V. *In vivo* dark-field reflection-mode photoacoustic microscopy. Opt Lett **30,** 625, 2005.
16. Hu, S., Maslov, K., and Wang, L.V. Second-generation optical-resolution photoacoustic microscopy with improved sensitivity and speed. Opt Lett **36,** 1134, 2011.
17. Hu, S., Maslov, K., and Wang, L.V. *In vivo* functional chronic imaging of a small animal model using optical-resolution photoacoustic microscopy. Med Phys **36,** 2320, 2009.
18. Sitharaman, B., Shi, X., Meijer, G.J., Liao, H., Walboomers, F., Jansen, J.J., *et al. In vivo* biocompatibility of ultra-short single walled carbon nanotube/biodegradable polymer nanocomposites for bone tissue engineering. Bone **43,** 362, 2008.
19. O'Connell, M.J., Bachilo, S.M., Huffman, C.B., Moore, V.C., Strano, M.S., Haroz, E.H., *et al.* Band gap fluorescence from individual single-walled carbon nanotubes. Science **297,** 593, 2002.

20. Prahl, S. Oregon medical laser center: optical absorption of hemoglobin. Online. 1999. Available at http://omlc.ogi.edu/spectra/hemoglobin/index.html

21. Ku, G., and Wang, L.V. Deeply penetrating photoacoustic tomography in biological tissues enhanced with an optical contrast agent. Opt Lett **30,** 507, 2005.

22. Kim, C., Erpelding, T.N., Jankovic, L., Pashley, M.D., and Wang, L.V. Deeply penetrating *in vivo* photoacoustic imaging using a clinical ultrasound array system. Biomed Opt Express **1,** 278, 2010.

23. Appel, A., Anastasio, M.A., and Brey, E.M. Potential for imaging engineered tissues with X-ray phase-contrast. Tissue Eng Part B **17,** 321, 2011.

24. Lungu, G.F., Li, M.-L., Xie, X.Y., Wang, L.V., and Stoica, G. *In vivo* imaging and characterization of hypoxia-induced neovascularization and tumor invasion. Int J Oncol **30,** 45, 2007.

25. Yao, J., Maslov, K., Shi, Y., Taber, L.A., and Wang, L.V. *In vivo* photoacoustic imaging of transverse blood flow by using Doppler broadening of bandwidth. Opt Lett **35,** 1419, 2010.

Address correspondence to:
Lihong V. Wang, Ph.D.
Optical Imaging Laboratory
Department of Biomedical Engineering
Washington University in St. Louis
One Brookings Drive
St. Louis, MO 63130

E-mail: lhwang@biomed.wustl.edu

Balaji Sitharaman, Ph.D.
Department of Biomedical Engineering
State University of New York at Stony Brook
Bioengineering Bldg., Room 115
Stony Brook, NY 11794

E-mail: balaji.sitharaman@stonybrook.edu